

# Constraint on the pulsar wind nebula scenario of origin of the TeV gamma ray emission from MGRO J2019+37 in the Cygnus region

Lab Saha\* and Pijushpani Bhattacharjee†

*AstroParticle Physics & Cosmology Division and Centre for AstroParticle Physics,  
Saha Institute of Nuclear Physics, 1/AF Bidhannagar, Kolkata 700064. India*

Origin of the TeV gamma ray emission from MGRO J2019+37 discovered by the Milagro experiment is investigated within the pulsar wind nebula (PWN) scenario using multiwavelength information on sources suggested to be associated with this object. We find that the PWN scenario is severely constrained by the upper limit on the radio flux from the region around MGRO J2019+37 given by the Giant Metrewave Radio Telescope (GMRT) as well as by the x-ray flux upper limit from SWIFT/XRT. Specifically, we find that within the synchrotron self-compton mechanism of production of TeV photons by electrons within the nebula, the GMRT and/or SWIFT/XRT flux upper limits impose upper limits of  $O(10^{-4} \text{ pc})$  on the effective characteristic size of the emission region within the PWN for an assumed distance of  $\sim$  few kpc to the source. This is about four orders of magnitude less than the characteristic size of the emission region typically invoked in explaining the TeV emission from a “standard” PWN such as the Crab Nebula.

## I. INTRODUCTION

The Cygnus region of the Galaxy hosts a number of extended, unidentified sources of TeV  $\gamma$ -ray emission, the most prominent of which is MGRO J2019+37 discovered by the Milagro experiment [1, 2]. Detailed analysis [3] of the observational data on this object collected during the period 2005–2008 gives a detection of this source with a statistical significance in excess of  $12\sigma$  between 1 and 100 TeV. The measured flux [3] from this source is  $7_{-2}^{+5} \times 10^{-10} \text{ s}^{-1} \text{ m}^{-2} \text{ TeV}^{-1}$  (with a  $\sim 30\%$  systematic uncertainty) at 10 TeV with a spectrum that is best described by a power-law with a spectral index of  $2.0_{-1.0}^{+0.5}$  (with a systematic uncertainty of  $\sim 0.1$ ) and an exponential cutoff at an energy  $E_c = 29_{-16}^{+50} \text{ TeV}$ .

Although no confirmed counterparts of the TeV source MGRO J2019+37 at lower energies are known, several possible associations with other observed sources have been suggested. The emission from MGRO J2019+37 may be due to either a single extended source or several unresolved sources. The EGRET sources 3EG J2021+3716 and 3EG J2016+3657 are positionally close to MGRO J2019+37, and thus could be the GeV counterparts of MGRO J2019+37 if it is a multiple source. At the same time, the EGRET source 3EG J2021+3716 is suggested to be associated with the radio and GeV pulsar PSR J2021+3651 (and its associated pulsar wind nebula PWN G75.2+0.1 [4, 5]) observed at GeV energies by AGILE (AGL J2020.5+3653) [6] as well as FERMI (OGL J2020.8+3649) [7]. A SWIFT/XRT observation [8] was also done within the positional uncertainty region of MGRO J2019+37 reported in [1, 2] and three x-ray sources were reported in the region with a total x-ray flux corresponding to  $\nu F_\nu \sim 8.1 \times 10^{-14} \text{ TeV cm}^{-2} \text{ s}^{-1}$  in the 2–10 keV energy region, which can, therefore, be taken as an upper limit on the possible x-ray flux from any x-ray counterpart of MGRO J2019+37 in this energy region. In addition, a wide-field deep radio survey of the MGRO J2019+37 region at 610 MHz was made by the Giant Metrewave Radio Telescope (GMRT) [9], yielding no detectable radio source, thus giving a conservative upper limit of  $\sim 1.0 \text{ mJy}$  on the radio flux from any point-like radio counterpart of MGRO J2019+37.

In this paper, we study the implications of a scenario in which the observed TeV  $\gamma$ -ray emission from MGRO J2019+37 arises from a Pulsar Wind Nebula (PWN) type source. Pulsar Wind Nebulae (PWNe) (see, e.g., [10] for a review), the most well-known example of which is the Crab Nebula (see [11] for a review), are known to be sources of very high energy gamma rays extending to TeV energies (see, e.g., [12, 13] for reviews). The very high energy (GeV – TeV) gamma rays are thought to be produced mainly through the so-called synchrotron self-compton mechanism, i.e., inverse Compton (IC) interaction of high energy electrons with low energy synchrotron photons emitted by the electrons themselves in the ambient magnetic field in the nebula. The photons constituting the cosmic microwave background (CMB) and infrared photons due to dust act as additional target photons for the IC scattering of the

\*Electronic address: lab.saha@saha.ac.in

†Electronic address: pijush.bhattacharjee@saha.ac.in

high energy electrons. The high energy electrons themselves are thought to be accelerated in the wind termination shock where the ultra-relativistic wind from the pulsar residing within the nebula is stopped by the nebular material. In principle, in addition to electrons high energy protons (and in general heavier nuclei) may be also accelerated [14–17], which can produce high energy photons through decay of neutral pions produced in inelastic  $p$ - $p$  collisions. In this paper we shall restrict our attention to emission only due to electrons. We use multiwavelength data and flux upper limits from observations in the region around MGRO J2019+37 including the radio upper limit given by GMRT [9], x-ray flux upper limit from SWIFT/XRT observations [8], GeV observations by FERMI [7], EGRET [18] and AGILE [6], and the TeV data from Milagro [1–3], to set constraints on the parameters of the emission model.

We find that the PWN scenario of origin of the observed TeV flux of MGRO J2019+37 is severely constrained by the upper limit on the radio flux from the region around MGRO J2019+37 given by the GMRT as well as by the x-ray flux upper limit from SWIFT/XRT. Specifically, the GMRT and/or SWIFT/XRT flux upper limits impose upper limits of  $O(10^{-4} \text{ pc})$  on the characteristic size of the emission region within the PWN for an assumed distance of  $\sim$  few kpc to the source. This is about four orders of magnitude less than the characteristic size of the emission region typically invoked in explaining the TeV emission from a “standard” PWN such as the Crab Nebula.

The reason for the upper limit on the size of the emission region in the PWN scenario is not hard to understand: Heuristically, ignoring for the moment the details of the energy spectrum of the electrons, let  $n_e$  be the number density of the electrons and  $r_{\text{em}}$  the characteristic radius of the (assumed spherical) emission region in the source. Recall that the TeV photons are produced through IC interaction of the nebular high energy electrons with primarily the synchrotron photons produced by the electrons themselves in the magnetic field in the nebular region. Since the number density of the synchrotron photons scales as  $n_e$ , the number density of the TeV photons produced by all the electrons roughly scales as  $n_e^2$ . Thus, for a given distance to the source, the emerging TeV flux from the source scales as  $n_e^2 r_{\text{em}}^2$ . The requirement of producing the observed TeV flux of MGRO J2019+37, therefore, fixes the product  $n_e r_{\text{em}}$ . On the other hand, the photon fluxes in the radio and x-ray regions scale with the product  $n_e r_{\text{em}}^2$  since those photons arise directly from synchrotron radiation of the electrons. Therefore, with the product  $n_e r_{\text{em}}$  fixed by the observed TeV flux of MGRO J2019+37, an upper limit on the radio flux given by GMRT or the x-ray flux given by SWIFT/XRT directly yields an upper limit on  $r_{\text{em}}$ . These arguments are elaborated upon more quantitatively in the following sections.

We organize this paper as follows: First, in Section II we specify the injection spectra of electrons that we use in this work to calculate the multiwavelength photon spectra within the context of the PWN scenario. Then in Section III we compare the resulting theoretically calculated multiwavelength photon spectra with the observed multiwavelength data and constraints pertaining to MGRO J2019+37, and discuss the implications for the PWN scenario of origin of the observed TeV flux from MGRO J2019+37. Finally, we summarize our results and conclude in Section IV.

## II. INJECTION SPECTRA OF ELECTRONS

Following the example of the Crab nebula, we shall assume that the nebula harbors two distinct populations of high energy electrons [14, 19]: (a) the “relic” (or “radio”) electrons whose synchrotron emission is responsible for the radio and FIR emission from the nebula, and (b) the “wind” electrons that, through their synchrotron emission, give rise to higher energy radiation extending to x-ray and gamma rays up to several hundred MeV. The radio electrons comprise of the electrons that were injected during the very early phase of rapid spin-down of the pulsar and which have since cooled down and accumulated within the nebula [20]. The wind electrons, on the other hand, are the ones that are being freshly accelerated at the pulsar wind termination shock and are being currently injected into the system. The IC interaction of the high energy wind electrons with the soft photons produced by the radio electrons as well as with CMBR and IR photons can then give rise to the observed multi-TeV emission. For simplicity, we work within the framework of the so-called “constant B-field” scenario [19, 21] and assume the magnetic field to be constant within the nebular region.

We take the following forms [19] for the radio and wind electron spectra,  $\frac{dn_e^r}{d\gamma}$  and  $\frac{dn_e^w}{d\gamma}$ , respectively:

$$\frac{dn_e^r}{d\gamma} = \begin{cases} A_e^r \gamma^{-\alpha_r} & \text{for } \gamma_{\min}^r \leq \gamma \leq \gamma_{\max}^r, \\ 0 & \text{otherwise,} \end{cases} \quad (1)$$

and

$$\frac{dn_e^w}{d\gamma} = A_e^w \exp\left(-\left[\frac{\gamma_{\min}^w}{\gamma}\right]^\beta\right) \times \begin{cases} \left(\frac{\gamma}{\gamma_b}\right)^{-\alpha_w}, & \text{for } \gamma < \gamma_b, \\ \left(\frac{\gamma}{\gamma_b}\right)^{-\alpha'_w}, & \text{for } \gamma_b \leq \gamma \leq \gamma_{\max}^w, \\ 0, & \text{for } \gamma > \gamma_{\max}^w. \end{cases} \quad (2)$$

The parameters  $A_e^r$ ,  $\alpha_r$ ,  $\gamma_{\min}^r$ ,  $\gamma_{\max}^r$ ,  $A_e^w$ ,  $\beta$ ,  $\alpha_w$ ,  $\alpha'_w$ ,  $\gamma_{\min}^w$ ,  $\gamma_{\max}^w$ , and  $\gamma_b$ , are to be determined by comparison of the resulting photon spectra with the observational data and multiwavelength constraints.

### III. MULTIWAVELENGTH PHOTON SPECTRA AND CONSTRAINTS

It is clear that, unlike in the case of the Crab Nebula for which the existence of detailed multiwavelength data allows one to determine the parameters of the model by performing detailed spectral fits to observational data [19], it is not practical or even meaningful to attempt to “determine” the parameters appearing in equations (1) and (2) for the PWN model of MGRO J2019+37 because of lack of such multiwavelength observational data. Instead, we shall focus on the plausible ranges of values of the most relevant parameters of the model by requiring that the resulting multiwavelength photon spectra be such as to be able to explain the observed TeV flux from MGRO J2019+37 without violating the upper limits on the x-ray and radio fluxes from the region around the object. In this exercise we shall be primarily guided by simple arguments of energetics based on the example of the Crab Nebula as a sort of “standard” PWN.

Let  $n_e^r$  and  $n_e^w$  in equations (1) and (2) denote the number densities of radio and wind electrons, respectively, and let  $r_{\text{em}}$  be the radius of the assumed spherical region within which the electrons are assumed to be distributed uniformly. Following the example of the Crab Nebula, we shall assume that the total energies contained in the radio and wind electrons,  $E_e^r = \frac{4}{3}\pi r_{\text{em}}^3 m_e c^2 \int \gamma \frac{dn_e^r}{d\gamma} d\gamma$  and  $E_e^w = \frac{4}{3}\pi r_{\text{em}}^3 m_e c^2 \int \gamma \frac{dn_e^w}{d\gamma} d\gamma$ , respectively, are comparable and roughly equal ( $\sim$  few  $\times 10^{48}$  erg) [19, 20]. This allows us to relate the normalization constants  $A_e^r$  and  $A_e^w$  appearing in equations (1) and (2), respectively, to each other and to the total energy content of the electrons,  $E_e = E_e^r + E_e^w$ , which, for a given set of the electron parameters,

$$\{\mathcal{P}\} \equiv \{\alpha_r, \gamma_{\min}^r, \gamma_{\max}^r, \beta, \alpha_w, \alpha'_w, \gamma_{\min}^w, \gamma_{\max}^w, \gamma_b\}, \quad (3)$$

can, therefore, be expressed as

$$E_e = \frac{4}{3}\pi r_{\text{em}}^3 A_e m_e c^2 \mathcal{F}(\{\mathcal{P}\}), \quad (4)$$

where  $\mathcal{F}$  is a calculable function of the set of parameters  $\{\mathcal{P}\}$ , the exact form of which need not concern us for the purpose of the discussions that follow.

Now, the energy spectrum of synchrotron photons produced by an electron of energy  $\gamma m_e c^2$  with a pitch angle  $\theta$  in a magnetic field  $B$  can be written as [22]

$$\mathcal{L}_\nu^{\text{Sy}} \equiv \left( \frac{d\mathcal{E}}{d\nu dt} \right)_{\text{Sy}} = \frac{\sqrt{3}e^3 B \sin \theta}{m_e c^2} \frac{\nu}{\nu_c} \int_{\nu/\nu_c}^{\infty} K_{5/3}(x) dx, \quad (5)$$

where  $e$  is the electron charge,

$$\nu_c = \frac{3e\gamma^2}{4\pi m_e c} B \sin \theta, \quad (6)$$

is the characteristic frequency of the emitted synchrotron radiation, and  $K_{5/3}(x)$  is the modified Bessel function of fractional order 5/3. In our calculations described below, we shall average over the electron pitch angle and adopt a value of  $\sin \theta = \sqrt{2/3}$  [19].

The number density,  $n_\nu^{\text{sy}}$ , of synchrotron photons produced per unit frequency at frequency  $\nu$  by all the electrons in the (assumed constant) magnetic field  $B$  in the spherical volume of radius  $r_{\text{em}}$  within the nebula can be expressed as

$$n_\nu^{\text{sy}} = \frac{1}{c h \nu} A_e^r g_{\text{sy}}(\nu, B, \{\mathcal{P}\}), \quad (7)$$

where  $g_{\text{sy}}(\nu, B, \{\mathcal{P}\})$  is a calculable function obtained by folding the electron spectra given in equations (1) and (2) with the synchrotron photon spectrum given by equation (5).

Similarly, the energy spectrum of photons produced by an electron of energy  $\gamma m_e c^2$  due to IC scattering off a background of soft photons is given by [22]

$$\mathcal{L}_\nu^{\text{IC}} \equiv \left( \frac{d\mathcal{E}}{d\nu dt} \right)_{\text{IC}} = \frac{3}{4} \frac{\sigma_T c}{\gamma^2} h^2 \nu \int_{h\nu/(4\gamma^2)}^{h\nu} d\epsilon \frac{n_b(\epsilon)}{\epsilon} f_{\text{IC}}(\epsilon, \nu, \gamma), \quad (8)$$

where  $\sigma_T$  is the Thomson cross section,  $h\nu$  is photon energy after scattering,  $n_b(\epsilon) d\epsilon$  is the number density of the background soft photons between energy  $\epsilon$  and  $\epsilon + d\epsilon$ , and

$$f_{\text{IC}}(\epsilon, \nu, \gamma) = 2q \ln q + (1+2q)(1-q) + \frac{1}{2} \frac{[4\epsilon\gamma q / (m_e c^2)]^2}{1 + 4\epsilon\gamma q / (m_e c^2)} (1-q),$$

with

$$q = \frac{h\nu}{4\epsilon\gamma^2 [1 - h\nu / (\gamma m_e c^2)]}.$$

Let  $n_\nu^{\text{IC}}$  denote the number density of high energy photons produced through IC process per unit frequency at frequency  $\nu$  by all the electrons in the spherical volume of radius  $r_{\text{em}}$  within the nebula. Within the context of the synchrotron self-compton scenario that we consider here, we can assume that the dominant target photons for the IC interaction of the high energy electrons that produce the TeV emission are the synchrotron photons produced by the electrons themselves, although the CMB and IR photons are additional targets.<sup>1</sup> Thus, with  $n_b$  replaced by  $n_\nu^{\text{sy}}$  in equation (8), and noting that  $n_\nu^{\text{sy}} \propto A_e^r$ , we see that  $n_\nu^{\text{IC}} \propto (A_e^r)^2$ , which allows us to write

$$n_\nu^{\text{IC}} = \frac{1}{c h \nu} (A_e^r)^2 g_{\text{IC}}(\nu, B, \{\mathcal{P}\}), \quad (9)$$

where  $g_{\text{IC}}(\nu, B, \{\mathcal{P}\})$  is another calculable function obtained by folding the the electron spectra given in equations (1) and (2) with the IC photon spectrum given by equation (8).

Thus, for the source at a distance  $D$ , the synchrotron radiation flux (energy/area/time/frequency) at frequency  $\nu$  at earth can be written as

$$\begin{aligned} F_\nu^{\text{sy}} &= \frac{1}{4\pi D^2} 4\pi r_{\text{em}}^2 n_\nu^{\text{sy}} c h \nu \\ &= \left( \frac{r_{\text{em}}}{D} \right)^2 A_e^r g_{\text{sy}}(\nu, B, \{\mathcal{P}\}), \end{aligned} \quad (10)$$

while the IC photon flux is

$$F_\nu^{\text{IC}} = \left( \frac{r_{\text{em}}}{D} \right)^2 (A_e^r)^2 g_{\text{IC}}(\nu, B, \{\mathcal{P}\}). \quad (11)$$

For a suitable choice of the magnetic field  $B$  and the parameter set  $\{\mathcal{P}\}$ , requiring that we be able to explain the observed TeV flux from MGRO J2019+37 at some energy, say, 10 TeV, by the IC flux (11), we get

$$A_e^r = \left( F_{10 \text{ TeV}}^{\text{MGRO}} \right)^{1/2} g_{\text{IC}}^{-1/2}(h\nu = 10 \text{ TeV}, B, \{\mathcal{P}\}) \frac{D}{r_{\text{em}}}, \quad (12)$$

where  $F_{10 \text{ TeV}}^{\text{MGRO}}$  is the observed flux from MGRO J2019+37 at 10 TeV. But, at the same time, we must ensure that, for the same value of  $B$  and the parameter set  $\{\mathcal{P}\}$ , the synchrotron flux given by equation (10) at  $\nu = 610 \text{ MHz}$  not exceed the radio flux upper limit given by GMRT [9],  $F_{610 \text{ MHz}}^{\text{GMRT}}$ , from the region around the observed position of MGRO J2019+37. This gives the condition

$$\left( \frac{r_{\text{em}}}{D} \right)^2 \leq F_{610 \text{ MHz}}^{\text{GMRT}} (A_e^r)^{-1} g_{\text{sy}}^{-1}(\nu = 610 \text{ MHz}, B, \{\mathcal{P}\}),$$

---

<sup>1</sup> In our full numerical calculations and results we include the CMB and IR photons in addition to the synchrotron photons.

which, upon substituting for  $A_e^r$  from equation (12) above, gives,

$$\left(\frac{r_{\text{em}}}{D}\right)_{\text{GMRT}} \leq F_{610 \text{ MHz}}^{\text{GMRT}} \left(F_{10 \text{ TeV}}^{\text{MGRO}}\right)^{-1/2} g_{\text{sy}}^{-1}(\nu = 610 \text{ MHz}, B, \{\mathcal{P}\}) g_{\text{IC}}^{1/2}(h\nu = 10 \text{ TeV}, B, \{\mathcal{P}\}). \quad (13)$$

In addition, we must ensure that for the same values of the parameter set  $\{\mathcal{P}\}$  and magnetic field  $B$  that account for the observed TeV flux, the predicted synchrotron flux given by equation (10) in the x-ray region at energy  $\sim 10$  keV not exceed the x-ray flux from the region (within the positional uncertainty) of MGRO J2019+37 reported by SWIFT/XRT observation [8],  $F_{10 \text{ keV}}^{\text{SWIFT/XRT}}$ . This gives

$$\left(\frac{r_{\text{em}}}{D}\right)_{\text{SWIFT/XRT}} \leq F_{10 \text{ keV}}^{\text{SWIFT/XRT}} \left(F_{10 \text{ TeV}}^{\text{MGRO}}\right)^{-1/2} g_{\text{sy}}^{-1}(h\nu = 10 \text{ keV}, B, \{\mathcal{P}\}) g_{\text{IC}}^{1/2}(h\nu = 10 \text{ TeV}, B, \{\mathcal{P}\}). \quad (14)$$

Thus, within the context of the PWN scenario of origin of the observed TeV emission from MGRO J2019+37, there is an upper limit to the size  $r_{\text{em}}$  of the emission region of the PWN for a given distance  $D$  to the source and a chosen set of the electron parameters  $\{\mathcal{P}\}$  and magnetic field  $B$  that yield the observed TeV flux of MGRO J2019+37. This upper limit,  $r_{\text{em},\text{max}}$ , is given by the lower of the right hand sides of equations (13) and (14).

The distance  $D$  to MGRO J2019+37 is not precisely known. The radio and GeV pulsar PSR J2021+3651, with its associated pulsar wind nebula PWN G75.2+0.1 [4–7], that has been suggested to be associated with MGRO J2019+37, is inferred to be at a distance of 3–4 kpc [23]. As we shall see, the constraint on  $r_{\text{em},\text{max}}$  will depend on the chosen distance of the source. Below, in our estimates of  $r_{\text{em},\text{max}}$  we shall allow a source distance range of 3 to 10 kpc.

For a given source distance  $D$ , one can choose the values of the electron parameters  $\{\mathcal{P}\}$  and magnetic field  $B$  such that the predicted fluxes in the radio and x-ray regions saturate the GMRT and SWIFT/XRT upper limits, respectively, while explaining the observed TeV flux. Examples of such multiwavelength photon spectra, which we obtain by performing a scan of the relevant parameters  $\{\mathcal{P}\}$  for three chosen values of the magnetic field  $B$ , are shown in Figure 1 for a choice of the source distance  $D = 3$  kpc. We have included the interstellar radiation field (ISRF) from Ref. [24] and the cosmic microwave background (CMB) in addition to the synchrotron photon field generated by the electrons themselves in obtaining the IC portion of the multiwavelength photon spectra (from x-ray to TeV energies) shown in Figure 1. The values of the electron parameters used in obtaining the curves in Figure 1 for the three chosen magnetic fields are listed in Table I where we also list the corresponding upper limits on the radius of the emission region,  $r_{\text{em},\text{max}}$ , and the total energy contained in electrons,  $E_e$ , in units of  $E_{e,\text{Crab}} = 5.3 \times 10^{48}$  erg [19]. As seen from Table I these upper limits on  $r_{\text{em}}$  are three or more orders of magnitude lower than the typical values of the characteristic size of the emission region ( $\sim 1$  pc) invoked in the PWN scenario of TeV emission of the Crab nebula, for example [19, 21].

Magnetic field $B$ ( $\mu\text{G}$ )	Electron parameters								$r_{\text{em},\text{max}}$ (pc)	$E_e / E_{e,\text{Crab}}$
	$\alpha_r$	$\gamma_{\text{min}}^r$	$\gamma_{\text{max}}^r$	$\beta$	$\alpha_w$	$\alpha'_w$	$\gamma_{\text{min}}^w$	$\gamma_{\text{max}}^w$		
0.3	1.37	1	$2.93 \times 10^5$	2.82	2.1	2.6	$4 \times 10^5$	$2 \times 10^9$	$2 \times 10^8$	$7.0 \times 10^{-4}$
3.0	1.67	1	$3 \times 10^5$	2.82	2.2	2.7	$4 \times 10^5$	$7 \times 10^8$	$2 \times 10^8$	$6.8 \times 10^{-5}$
125	1.75	1	$1.5 \times 10^5$	2.82	2.3	2.8	$2 \times 10^5$	$1.0 \times 10^8$	$8 \times 10^7$	$2.2 \times 10^{-6}$

TABLE I: Values of the electron parameters used in obtaining the curves shown in Figure 1 for the three chosen values of the magnetic field. The corresponding upper limits on the radius of the emission region,  $r_{\text{em},\text{max}}$ , and the total energy contained in electrons,  $E_e$ , in units of  $E_{e,\text{Crab}} = 5.3 \times 10^{48}$  erg, are also given. The source distance is taken as  $D = 3$  kpc.

A heuristic estimate of the value of  $r_{\text{em},\text{max}}$  for MGRO J2019+37 can be obtained just by comparing the constrained spectral energy distribution (SED) of MGRO J2019+37 shown in Figure 1 with the SED of the Crab nebula also shown in the same Figure. Note that Crab emits comparable amount of energy at TeV and radio wavelengths, with  $\nu F_{\nu}^{\text{Crab}}(h\nu = 10 \text{ TeV}) \simeq 1.5 \times 10^{-11} \text{ erg cm}^{-2} \text{ s}^{-1}$  and  $\nu F_{\nu}^{\text{Crab}}(\nu = 610 \text{ MHz}) \simeq 0.74 \times 10^{-11} \text{ erg cm}^{-2} \text{ s}^{-1}$  at 10 TeV and 610 MHz, respectively, for example. In contrast, for MGRO J2019+37, while the energy emitted at TeV energies is comparable with that for Crab, with  $\nu F_{\nu}^{\text{MGRO}}(h\nu = 10 \text{ TeV}) \simeq 1.1 \times 10^{-11} \text{ erg cm}^{-2} \text{ s}^{-1}$ , the GMRT upper limit restricts the possible flux of MGRO J2019+37 in the radio region to  $\nu F_{\nu}^{\text{MGRO}}(\nu = 610 \text{ MHz}) \simeq 6.1 \times 10^{-18} \text{ erg cm}^{-2} \text{ s}^{-1}$ , about 6 orders of magnitude less than the corresponding quantity for Crab at that frequency.

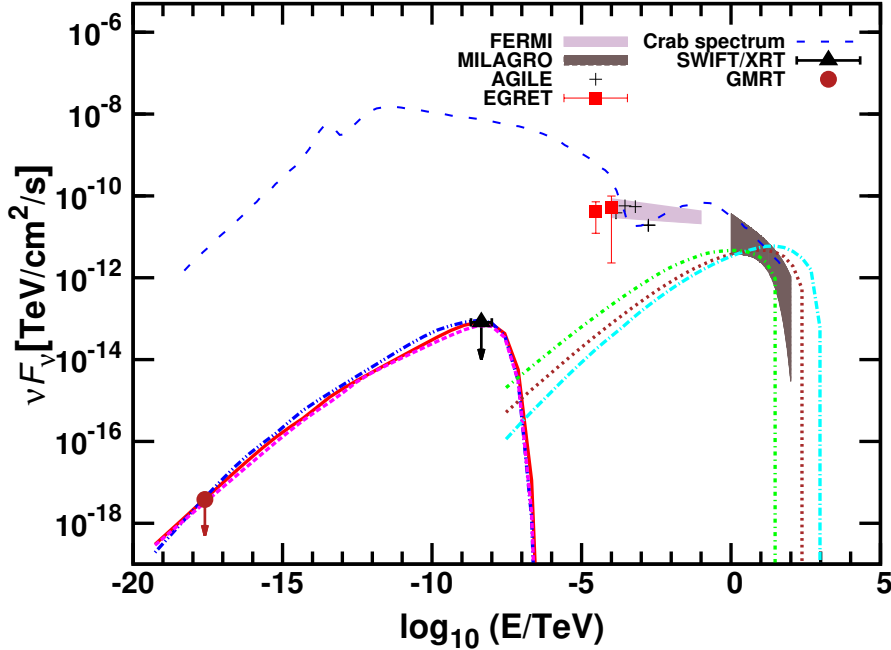


FIG. 1: The constrained spectral energy distribution (SED) of MGRO J2019+37 from radio to TeV region in the PWN scenario. The solid, dash-double-dotted and dashed curves from radio to x-ray energies are the synchrotron spectra for magnetic fields of  $B = 3$  and  $0.3$  and  $125 \mu\text{G}$ , respectively, and the dotted, long-dash-dotted and dot-dashed curves from the x-ray to TeV energies are the corresponding inverse Compton (IC) spectra for the three magnetic fields, respectively. The values of the various parameters of the electron spectra [see equations (1) and (2)] corresponding to the three magnetic fields are listed in Table I. The distance to the source is taken to be  $D = 3 \text{ kpc}$ . Multiwavelength observational data and flux constraints from observations in the region around MGRO J2019+37 including the radio upper limit given by GMRT [9], x-ray flux upper limit from SWIFT/XRT observations [8], GeV observations by FERMI [7], EGRET [18] and AGILE [6] and TeV observations by Milagro [1–3] are shown. In addition, the SED of the Crab nebula (at a distance of  $\sim 2 \text{ kpc}$ ) from radio to TeV energies (taken from Ref. [19]) is also shown for comparison.

Let us define the ratio

$$\xi \equiv \frac{\nu F_\nu^{\text{IC}}(h\nu = 10 \text{ TeV})}{\nu F_\nu^{\text{sy}}(\nu = 610 \text{ MHz})}, \quad (15)$$

where  $F_\nu^{\text{sy}}$  and  $F_\nu^{\text{IC}}$  are given by equations (10) and (11), respectively. Let us demand that the measured TeV flux of both Crab and MGRO J2019+37 be explained by the synchrotron self-compton (i.e., IC) process within the PWN scenario. Then, for a given set of the electrons' spectral parameters  $\{\mathcal{P}\}$  and magnetic field  $B$ , assumed same for the moment for both Crab and MGRO J2019+37, it is easy to see, using equations (15), (10), (11) and (12), that

$$\left(\frac{r_{\text{em}}}{D}\right)_{\text{Crab}} \xi_{\text{Crab}} = (F_{10 \text{ TeV}}^{\text{Crab}}/F_{10 \text{ TeV}}^{\text{MGRO}})^{1/2} \left(\frac{r_{\text{em}}}{D}\right)_{\text{MGRO}} \xi_{\text{MGRO}}, \quad (16)$$

where the sub(super)scripts Crab and MGRO refer to quantities relevant to Crab and MGRO J2019+37, respectively.

Now, from the above discussions of comparison of the measured SED of Crab and the constrained SED of MGRO (see Figure 1), we see that  $\xi_{\text{Crab}} \simeq 2$  and  $F_{10 \text{ TeV}}^{\text{Crab}}/F_{10 \text{ TeV}}^{\text{MGRO}} \simeq 1$ , whereas  $\xi_{\text{MGRO}} \geq 1.8 \times 10^6$ . Using these estimates in equation (16) we immediately get the constraint

$$\left(\frac{r_{\text{em}}}{D}\right)_{\text{MGRO}} \leq 1.1 \times 10^{-6} \times \left(\frac{r_{\text{em}}}{D}\right)_{\text{Crab}}, \quad (17)$$

which, upon using typical numbers for the relevant quantities pertaining to Crab and MGRO J2019+37, yields

$$(r_{\text{em}})_{\text{MGRO}} \leq 1.7 \times 10^{-6} \text{ pc} \left(\frac{D}{3 \text{ kpc}}\right)_{\text{MGRO}} \left(\frac{r_{\text{em}}}{1 \text{ pc}}\right)_{\text{Crab}} \left(\frac{2 \text{ kpc}}{D}\right)_{\text{Crab}}. \quad (18)$$

It is thus seen that if MGRO J2019+37 is like a “standard” PWN with the spectral parameters of its electron population and the magnetic field similar to those of Crab nebula, then within the context of the synchrotron self-compton scenario of production of TeV photons, the MGRO J2019+37 has to be a significantly more compact source than a standard PWN like the Crab. Of course, the electron parameters and the magnetic field inside MGRO J2019+37 have no reason to be exactly same as those in Crab. However, this does not alter the above general inference, the main reason for which is the strong constraints on the radio and x-ray fluxes from MGRO J2019+37 imposed by the GMRT and the SWIFT/XRT observations discussed above in relation to those of Crab at these energies (see Figure 1).

Note that the constraint on  $r_{\text{em}}$  of MGRO J2019+37 given by equation (18), derived analytically under the assumption that the values of the electrons’ spectral parameters  $\{\mathcal{P}\}$  and the magnetic field are same as those of Crab, is fairly close to the value  $r_{\text{em},\text{max}} \simeq 2.2 \times 10^{-6}$  pc displayed in Table I for the case of magnetic field  $B = 125 \mu\text{G}$  typically invoked for the Crab [19]. The difference may be attributed to the different values of the electrons’ spectral parameters adopted for MGRO J2019+37 in comparison with those for the Crab.

To see the dependence of  $r_{\text{em},\text{max}}$  on the electron parameters  $\{\mathcal{P}\}$  and magnetic field  $B$ , we show in Figure 2 the variations of  $r_{\text{em},\text{max}}$  given by equations (13) and (14) with some of the relevant parameters of the electrons with respect to which the variations of  $r_{\text{em},\text{max}}$  are most sensitive. In Figure 2, for illustration, the electron parameters are individually varied about their respective values shown in Table I for the case of  $B = 0.3 \mu\text{G}$  and source distance  $D = 3 \text{kpc}$ . The crossing points of the two curves in each panel in Figure 2 correspond to the parameter values for which the GMRT and the SWIFT/XRT bounds are simultaneously saturated (see Figure 1). It is seen that the requirement of simultaneously respecting the two constraints given by equations (13) and (14) restricts  $r_{\text{em},\text{max}}$  to values less than a few  $\times 10^{-4}$  pc for all reasonable values of the magnetic field within the nebula.

As seen from Figure 2, the most significant variation of  $r_{\text{em},\text{max}}$  occurs not with respect to the electron parameters, but rather with respect to the magnetic field  $B$ . In general,  $r_{\text{em},\text{max}}$  is larger for smaller magnetic fields. In Figure 3 we show the variations of the lower of the two  $r_{\text{em},\text{max}}$  values given by equations (13) and (14) and the corresponding variation of the total electron energy ( $E_e$ ) with magnetic field  $B$  for various source distance  $D$ , with the values of the electron parameters kept fixed at those given in Table I for the case of  $B = 0.3 \mu\text{G}$ . As expected, and as seen from the right panel of Figure 3, the total energy in electrons required to produce the observed TeV flux is larger for smaller magnetic fields as well as for larger distance to the source. However, for too small values of magnetic field, the density of synchrotron photons of the requisite energy becomes so low that the synchrotron self-compton (IC) mechanism of explaining the TeV flux becomes inefficient unless the total energy content of electrons is made several orders of magnitude larger than that for Crab.

In the above discussions we have made the simplifying assumption of the electrons — and consequently the photons generated by them — being uniformly distributed within a spherical “emission region” of radius  $r_{\text{em}}$  within the nebula. More realistically, the radius  $r_{\text{em}}$  may be considered as a kind of characteristic length scale of a possible non-uniform spatial distribution of the electrons and/or the photons generated by them [19, 21]. Also, the magnetic field inside the nebula is likely to be not spatially constant, but rather varying with a characteristic length scale similar to  $r_{\text{em}}$ . These details, however, are unlikely to change the general conclusion regarding the extreme compactness of the emission region of MGRO J2019+37 relative to a Crab nebula-like PWN within the general PWN scenario of origin of the observed TeV emission from the MGRO J2019+37.

#### IV. SUMMARY AND CONCLUSIONS

To summarize, in this paper we have considered a PWN scenario of the origin of the observed TeV gamma ray emission from MGRO J2019+37. We find that, while no lower energy counterparts of this object have yet been identified, the upper limits on possible radio and x-ray emissions from sources suggested to be associated with MGRO J2019+37 already provide rather strong constraints on the size of the emission region of the nebula, with the characteristic radius of the emission region being restricted to  $O(10^{-4})$  pc, about four orders of magnitude less than that of the Crab nebula. This conclusion is in fact fairly general and is reasonably independent of the details of the parameters describing the spectrum of the electrons responsible for the emission and the magnetic field within the nebula as long as the total energy content of the electrons is not too large compared to that for the case of the Crab nebula.

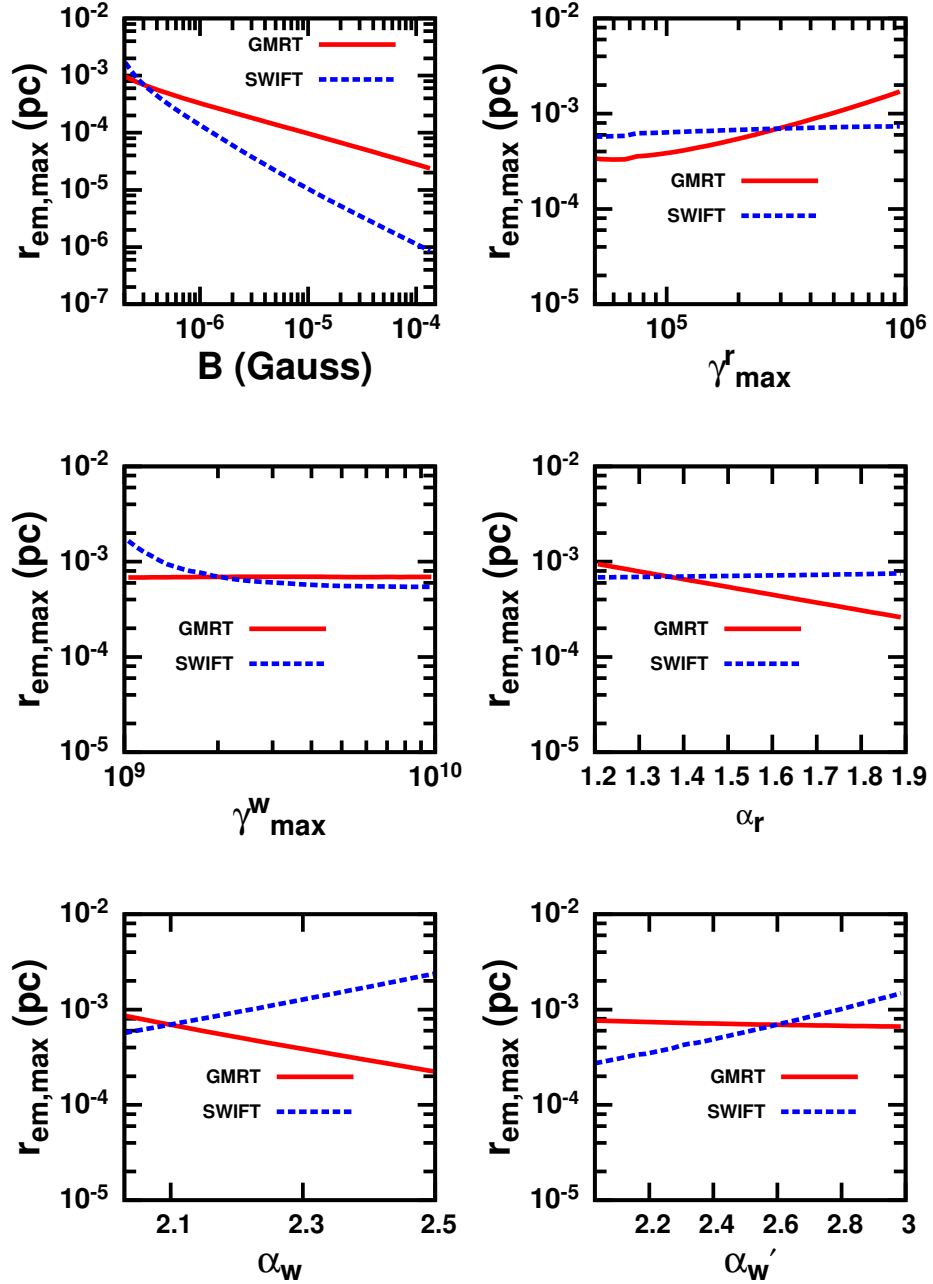


FIG. 2: Variation of  $r_{\text{em},\text{max}}$  with magnetic field and various electron parameters about their respective values for the case  $B = 0.3 \mu\text{G}$  shown in Table I. The source distance is  $D = 3 \text{ kpc}$ . The crossing points of the two curves in each panel correspond to the parameter values for which the GMRT and the SWIFT/XRT bounds are simultaneously saturated (see Figure 1).

---

[1] A.A. Abdo et al., *Astrophys. J.* 658 (2007) L33.  
[2] A.A. Abdo et al., *Astrophys. J.* 664 (2007) L91.  
[3] A.A. Abdo et al., *Astrophys. J.* 753 (2012) 159.  
[4] M.S.E. Roberts et al., *Astrophys. J.* 577 (2002) L19.  
[5] J.W.T. Hessels et al., *Astrophys. J.* 612 (2004) 389.  
[6] J.P. Halpern et al., *Astrophys. J.* 688 (2008) L33.

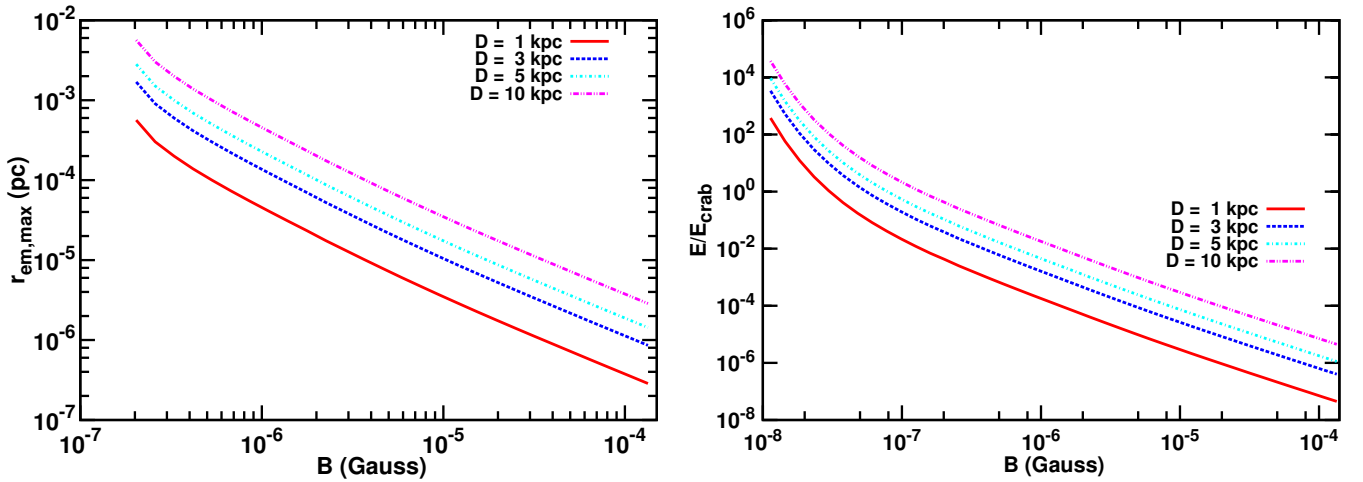


FIG. 3: Variation of  $r_{\text{rem,max}}$  and the corresponding total energy in electrons ( $E_e$ , in units of  $E_{e,\text{Crab}} = 5.3 \times 10^{48}$  erg) with magnetic field ( $B$ ), for various source distance  $D$ . The values of the electron parameters are kept fixed at those given in Table I for the case of  $B = 0.3 \mu\text{G}$ .

- [7] A.A. Abdo et al., *Astrophys. J. Suppl.* 183 (2009) 46.
- [8] R. Landi et al., *Astronomer's Telegram* #1097, June 2007.
- [9] J.M. Paredes et al., *Astron. Astrophys.* 507 (2009) 241.
- [10] B.M. Gaensler and P.O. Slane, *Annu. Rev. Astron. Astrophys.* 44 (2006) 17.
- [11] J.J. Hester, *Annu. Rev. Astron. Astrophys.* 46 (2008) 127.
- [12] F.A. Aharonian, *Very High Energy Cosmic Gamma Radiation: A crucial window on the extreme universe*, World Scientific (Singapore, 2004).
- [13] O. Kargaltsev, G.G. Pavlov, and M. Durant, arXiv: 1207.1681.
- [14] A.M. Atoyan and F.A. Aharonian, *Mon. Not. Roy. Astron. Soc.* 278 (1996) 525.
- [15] W. Bednarek and R.J. Protheroe, *Phys. Rev. Lett.* 79 (1997) 2616.
- [16] E. Amato, D. Guetta, and P. Blasi, *Astron. Astrophys.* 402 (2003) 827.
- [17] W. Bednarek and M. Bartosik, *Astron. Astrophys.* 405 (2003) 689.
- [18] R.C. Hartman et al., *Astrophys. J. Suppl.* 123 (1999) 79.
- [19] M. Meyer, D. Horns, and H.-S. Zechlin, *Astron. Astrophys.* 523 (2010) A2.
- [20] A.M. Atoyan, *Astron. Astrophys.* 346 (1999) L49.
- [21] A.M. Hillas et al., *Astrophys. J.* 503 (1998) 744.
- [22] G.R. Blumenthal and R.J. Gould, *Rev. Mod. Phys.* 42 (1970) 2.
- [23] A. Van Etten, R.W. Romani, and C.-Y. Ng, *Astrophys. J.* 680 (2008) 1417.
- [24] J.S. Mathis, P.G. Mezger, and N. Panagia, *Astron. Astrophys.* 128 (1983) 212.